Korean J. Chem. Eng., 36(2), 173-185 (2019)
DOI: 10.1007/s11814-018-0193-7

pISSN: 0256-1115
eISSN: 1975-7220

INVITED REVIEW PAPER

Nanostructured colloidal quantum dots for efficient electroluminescence devices

Wan Ki Bae* and Jaehoon Lim,†**

*SKKU Advanced Institute of Nano Technology (SAINT), Sungkyunkwan University, Suwon, Gyeonggi-do 16419, Korea
**Department of Chemical Engineering & Department of Energy System Research, Ajou University, Suwon, Gyeonggi-do 16499, Korea

(*Received 21 August 2018 • accepted 14 November 2018*)

Abstract−The exceptional quality of light generated from colloidal quantum dots has attracted continued interest from the display and lighting industry, leading to the development of commercial quantum dot displays based on the photoluminescence down-conversion process. Beyond this technical level, quantum dots are being introduced as emissive materials in electroluminescence devices (or quantum dot-based light-emitting diodes), which boast high internal quantum efficiency of up to 100%, energy efficiency, thinness, and flexibility. In this review, we revisit various milestone studies regarding the core/shell heterostructures of colloidal quantum dots from the viewpoint of electroluminescence materials. Development of nanostructured colloidal quantum dots advanced from core/shell heterostructure, core/thick shell formulation, and delicate control of confinement potential shape has demonstrated close correlation of the photophysical properties of quantum dots with the performance of electroluminescence device, which provided useful guidelines on the heterostructured quantum dots for mitigating or eliminating efficiency limiting phenomena in quantum dot light emitting diodes. To enable practical and high performance quantum dot-based electroluminescence devices in the future, integration of design concepts on the heterostructures with environmentally benign systems will be crucial.

Keywords: Colloidal Quantum Dots, Nanocrystals, Core/Shell Heterostructures, Electroluminescence, Light Emitting Diodes

INTRODUCTION

Colloidal quantum dots (QDs), nanosized semiconductor crystals comprising 100 s to 10,000 s of atoms, have been studied for more than 20 years due to their unique optical properties, such as broadband absorption but narrow emission bandwidth, controllable band gap from ultraviolet to infrared, and high photoluminescence quantum yield (PL QY) close to unity [1,2] (Fig. 1). Ongoing efforts towards QD synthesis have recently achieved a very narrow PL bandwidth down to 20-30 nm in full-width at half maximum for CdSe QDs, which encourages the commercialization of QD-based displays based on PL down conversion [converting blue light from inorganic light emitting diodes to red and green using QDs; i.e. QD enhancement film (QD-EF)] [3].

Despite the successful commercialization of QD displays, there is no doubt that the ultimate technical solution for QD displays is electroluminescence (EL)-based devices. EL represents the generation of light converted directly from electrical energy. More specifically, EL results from the radiative recombination of electron and hole pairs (exciton) in semiconductors in which the charges are provided from the anode (hole) and cathode (electron). An EL device employing QDs as emissive materials (known as quantum dot-based light-emitting diodes, QLEDs) are characterized by thinness, lightness, and flexibility when fabricated on a variety of substrates (e.g., glass, plastic, or fabric). In addition, they boast better energy efficiency than liquid crystal displays (LCDs) that inevitably lose a large fraction of light (~90%) through the polarizer and liquid crystal layer. These benefits have led to intense research on high-quality QD synthesis [4-8] and QLED device physics [9-12] over the last 20 years. Consequently, we have seen significant improvements in device performance in terms of external quantum efficiency (EQE), which has reached 20%, close to its theoretical maximum [13-17]. For details about the development history of QLEDs and recent achievement on device performance and emerging applications, refer to several review articles [1,2,18-20].

In this review, we revisit milestone research on QLED technology from the viewpoint of QD heterostructures and their spectroscopic behavior in devices. Based on the fundamental working principle of QLEDs, we introduce important design concepts of QDs and research illustrating how QD heterostructures can overcome efficiency-limiting photophysical processes in QLEDs. Finally, we discuss future research directions of QDs towards the commercialization of QLEDs.

OPERATION OF QLEDs AND EFFICIENCY DETERMINING FACTORS

Modern QLEDs employ a *p*-i-*n* heterojunction diode structure composed of an anode/hole injection layer (HIL)/hole transport layer (HTL)/QD emissive layer (EML)/electron transport layer (ETL)/electron injection layer (EIL)/cathode (Fig. 2(a)), in which HIL (EIL) assists carrier injection from electrodes to HTL (ETL) and HTL

†To whom correspondence should be addressed.
E-mail: jhlim@ajou.ac.kr

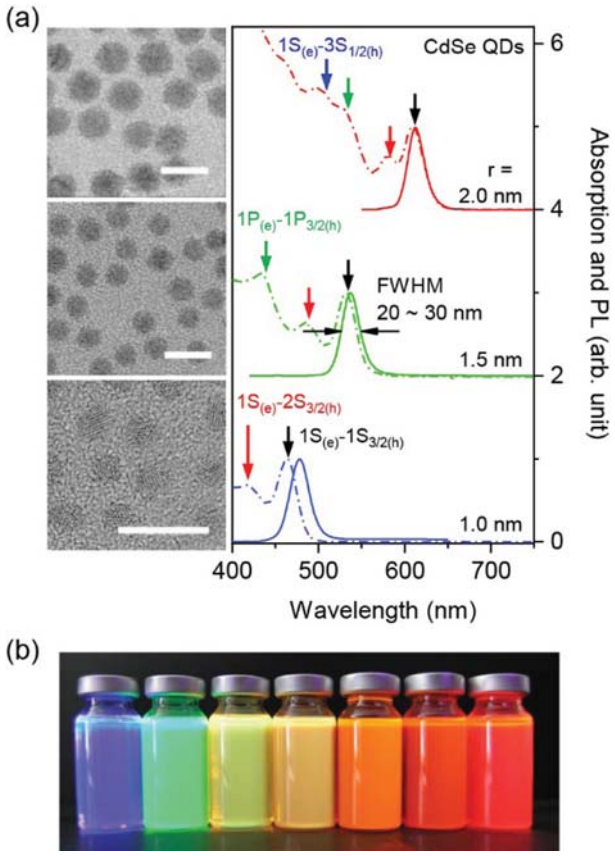

Fig. 1. (a) (left) Transmission electron microscopy images (left, scale bar: 10 nm) and (right) their absorption (dash-dot) and photoluminescence (PL) spectra (solid) of size-controlled CdSe QDs with varying sizes [radius (r)=1.0, 1.5, and 2.0 nm from the bottom]. Electronic transitions observed in their absorption spectra are encoded as colored arrows. (b) Photograph of QDs with various band gaps under ultraviolet light.

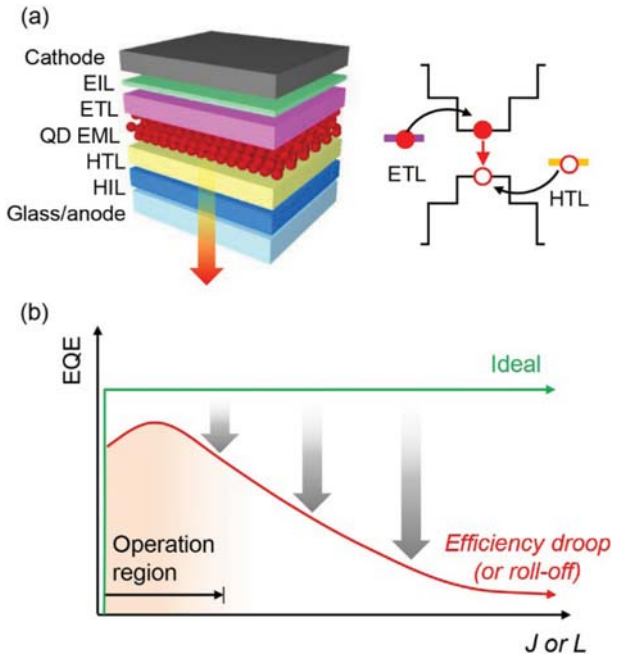

Fig. 2. (a) (left) A schematic illustration of *p*-i-*n* QLED structure and (right) exciton formation process within QDs in devices. Electrons (holes) from the cathode (anode) delivered from electron (hole) transport layers that generate excitons within an emission layer comprised of QDs. (b) Ideal (green) and typical (red) EQE curves of QLEDs as a function of current density (J) or luminance (L). Real QLEDs exhibit a peak EQE value at low J (shaded region) and progressive deterioration of efficiency with increasing J, known as the efficiency droop (or roll-off).

(ETL) in delivering charge carriers from the anode (cathode) to QDs under applied bias. At the charge transport layer (CTL)-QD interface, the electron and hole are tunneled into the QDs through potential barriers resulting from an energy level difference between transport levels of HTL and valence band (VB) of QDs, ETL and conduction band (CB) of QDs, a wide band gap shell (see section 2), and insulating surface ligands. The injected carriers generate photons by radiative recombination corresponding to the band gap of QDs.

Since an initial demonstration in 1994 [21], the device performance of QLEDs has rapidly improved in only ~20 years. For example, the peak EQE of red QLEDs recorded a peak external quantum efficiency (EQE, ratio of the number of emitted photons from the device front to the number of injected carriers) of approximately 2% in 2009 [22], which increased to the theoretical maximum (approximately 20%) for all primary colors [14-17]. Also, their maximum brightness reached the level of modern organic light emitting diodes, for example, 106,000 cd m^{-2} for red [23], 460,000 cd m^{-2} for green [24], and 7,600 cd m^{-2} for blue [25]. As well as these metrics of efficiency and optical output, the optical quality of emission spectra are also notable. Advances in QD synthesis allow the fabrication of high-quality QDs with exceptional size and shape uniformity, which leads to narrow spectral emission bandwidths for QD ensembles, close to those of individual QDs (FWHM ~20 nm) [2]. Excellent color purity in QLEDs is particularly important for next generation displays, which should meet Recommendation 2020 [2], an industrial standard describing the extended color representation range.

Such rapid progress originates from advances in QD synthesis and vigorous research on QLED structures, motivated by the fundamental principles of organic LEDs. In particular, the introduction of metal oxide ETLs (e.g., ZnO [26] and TiO_2 [27,28]) in combination with organic HTLs initially adopted by Stouwdam et al. [26] led to a great leap in QLED performance. For instance, ZnO nanoparticle ETL has an appropriate band gap position (~4 eV of CB and ~7.3 eV of VB), which enables the transport of electrons to CB of various QDs and the blockage of hole leakage from QD/HTL [29]. In addition, the structural robustness of ZnO film against various organic solvents enables QLED fabrication by solution-based orthogonal processing. Through continued study and optimization, QLEDs with hybrid CTLs have become a mainstream state-of-the-art QLED owing to their exceptionally high EQE and brightness [13-16,23,25,29].

Emission resulting from QDs would be almost identical whether produced by optical pumping in QD-EF or by electrical pumping

in QLEDs because the energy of the photon depends on the energy gap between VB and CB, defined as the band gap. However, QDs in PL devices and EL devices experience completely different exciton formation processes, nanoscopic morphology, and consequent complexity of photophysical processes. While optical pumping produces excitons by the optically allowed transition of electrons residing in the VB to CB and all processes occur *inside* QDs, electrical pumping produces excitons through direct injection of carriers from *outside* to the band-edge states of QDs. In terms of nanoscopic morphology, QDs in QD-EF are homogeneously dispersed in insulating polymer matrices [30,31] to minimize dot-to-dot interaction. In contrast, QLEDs generally contain closely packed QD layers as the emissive layer. The proximity of QDs leads to very efficient energy transfer between QDs and complicates our understanding of the photophysical mechanisms behind the QD EL. From all these complexities arise additional considerations to understand and quantify the EL of QLEDs.

In general, LED performance is evaluated using photometric figures of merit, such as lumen (lm), luminance (cd m^{-2}), or luminous efficacy (lm W^{-1}), which convert radiometric quantities based on a non-uniform, bell-shaped human eye sensitivity curve [2] centered at 555 nm. Instead of such color-dependent metrics, quantum efficiency, the ratio of the number of photons generated to the number of injected carriers, widely assesses device performance. The EQE (η_{EQE}) is defined by the following expression: $\eta_{EQE}=\eta_{IQE}\eta_{out}=\chi\eta_{inj}\eta_{QY}\eta_{out}$, where η_{IQE} is the internal quantum efficiency (IQE, $\eta_{IQE}=\chi\eta_{inj}\eta_{QY}$), η_{out} is the outcoupling efficiency defining the fraction of photons escaped from the device (η_{out}=20% for typical planar EL devices with a reflective electrode and active layers with refractive indices of 1.6-1.8 [32]), χ is the fraction of excitons enabling spin-allowed transition, η_{inj} is the fraction of excitons generated in QDs to the injected carriers, and η_{QY} is the luminescence quantum yield (QY) of QD EML. While the achievement of theoretical maximum efficiency implies that all variables in the expression can reach unity, in most cases the EQE is rarely maintained over varied device operation conditions. Instead, the EQE curves typically show a peak at low current and a gradual decrease with higher current, known as the efficiency droop or roll-off (Fig. 2(b)).

Among the variables in this expression, fortunately, QDs promise a unity of χ for electrically pumped excitons. While optical pumping always produces optically active excitons with a total spin state of 0 (i.e., singlet), the electrical pumping that separately injects an electron and a hole can generate either a total spin state of 0 (25%) or 1 (triplet, 75%) and the selection rule forbids the optical transition of the triplet states. As a result, the statistics of the electrically pumped exciton limit χ=0.25. For colloidal QDs, however, such restriction originating from spin statistics can be relaxed by efficient intersystem crossing due to minimal singlet-triplet energy spacing less than kT (ca. 26 meV). As a representative example, spherical CdSe QDs with hexagonal crystal structure split the band-edge $1S_{(e)}$-$1S_{3/2(h)}$ state (black arrows in Fig. 1(a)) into five manifolds with total angular momenta $|N_m|=0^U, 1^U, 0^L, 1^L$, and 2 due to the crystal field of the wurtzite lattice, shape asymmetry, and electron-hole exchange [33,35] (Fig. 3(a) and 3(b)). The optically for-

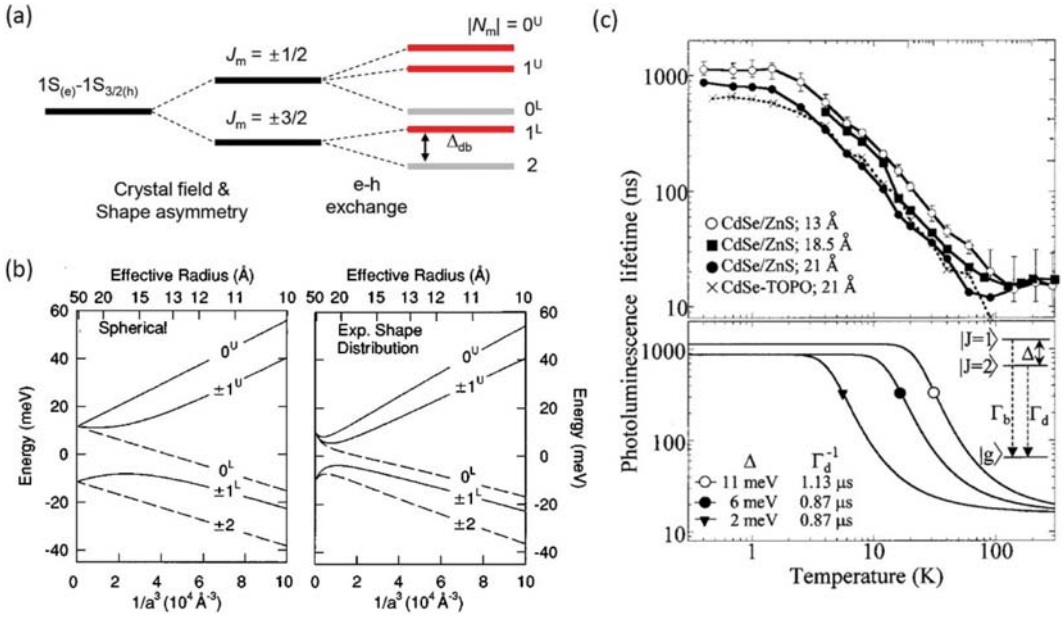

Fig. 3. (a) $1S_{(e)}$-$1S_{3/2(h)}$ band-edge fine structure of CdSe QDs, evolved to five states with overall angular momentum quantum numbers ($|N_m|$)=0^U, 1^U, 0^L, 1^L, and 2. Optically passive and active states are indicated by grey and red lines, respectively. (b) Computation of the exciton band-edge structure of wurtzite CdSe QDs with ellipticity μ=0 (spherical dots, left) and μ=0.086 (slightly prolate estimated from samples, right). Solid (dashed) lines indicate optically active (passive) transitions. Adapted with permission from ref. [33]. Copyright 1996 American Physical Society. (c) (top) Observation of temperature dependent exciton lifetime for CdSe QDs with three different radii. All measurements reveal an almost size-independent onset of exciton decay at ~2 K. (bottom) Calculated temperature dependence of exciton lifetime (t) for different Δ_{db}. Simplified two-level states with spacing, Δ_{db}, and Boltzmann statistics of exciton occupation were introduced to this model. (c). Adapted with permission from ref. [34]. Copyright 2003 AIP Publishing.

bidden lowest exciton state (i.e., dark exciton) is related to $|N_m|=2$, and the next optically allowed exciton state (i.e., bright exciton) is $|N_m|=1^L$. Separation between the two states is defined as the dark-bright exciton splitting energy Δ_{db}. Even though the occupation of a lower dark exciton state is thermally favorable according to Boltzmann statistics, a small Δ_{db} ranging from ~1 meV to ~20 meV [35-37] (see Fig. 3(b) and 3(c) for details) allows effective mixing between these two lowest states even at room temperature, thereby fulfilling χ=1. This advantage of band-edge fine structures has also been found in other QDs that are being actively researched. For instance, temperature dependent PL decay reveals that InP QDs also exhibit very small Δ_{db} less than 15 meV [38,39]. Even cesium lead halide perovskite ($CsPbX_3$, X=Cl, Br, and I) QDs reveal unique bright triplet states induced by strong spin-orbit coupling in combination with the Rashba effect [40]. As a result, QD-based EL makes it possible to achieve internal quantum efficiency (η_{int}) of 100%, which is a major difference from organic LEDs that require a complicated design of molecular structures to harvest triplet excitons (i.e., inducing spin-orbit coupling by introducing heavy metals [41-43] or minimizing singlet-triplet energy spacing to less than kT to promote intersystem crossing [44,45]) for high internal efficiency.

Therefore, considering the unity of χ, the current dependent behavior of EQE is a result of other efficiency variables, in particular, η_{QY}. Thin QD EMLs (typically, 1-2 monolayers) containing electrically isolated states prevent a shift of the exciton recombination zone under various applied biases, so η_{out} is mainly determined by the device structure (e.g., thickness of CTLs and EML, ITO/glass, refractive index of layers, and reflective electrodes [46]) that are not dependent on device operation. In the following sections, we discuss point-by-point the efficiency limiting factors of QLEDs and how the engineered core/shell heterostructures can overcome or mitigate undesirable drops in efficiency. As well as achieving high PL QY of QDs, delicate control of the internal structure of QDs and morphology control are also essential to alleviate the efficiency reduction processes. Spectroscopic analysis of QDs dispersed in solution as well as in devices reveals a close connection between the photophysical property of core/shell heterostructured QDs and device characteristics.

TYPE-I CORE/SHELL HETEROSTRUCTURES

In colloidal QDs, the radiative decay rate of excitons (k_r) is typically very fast owing to the confined geometry ($\tau_r=1/k_r$=several to 10 s ns) [33,47]; however, this process is prone to be interfered by sparse electronic states located between VBM and CBM, known as defect states. From an atomistic viewpoint, the crystal lattice of an inorganic nanocrystal loses its periodicity at the interface between the nanocrystal surface and its surroundings, which exposes unsaturated atoms on the surface. Empty orbitals (the S orbital of Cd atoms on CdSe QDs) or electron pairs (the P orbital of Se atoms on CdSe QDs) belonging to surface atoms provide electronic states accessible to carriers. Namely, they accept photo or electrically generated carriers and lose their energy by heat instead of the radiative recombination of excitons. Because of this, defect states originating from surface dangling bonds are also called surface defects. Besides the surface states, internal defects formed during synthesis (misfit dislocation or point defect) can also contribute to the nonradiative decay process.

Empirically, side processes impeding radiative decay are classi-

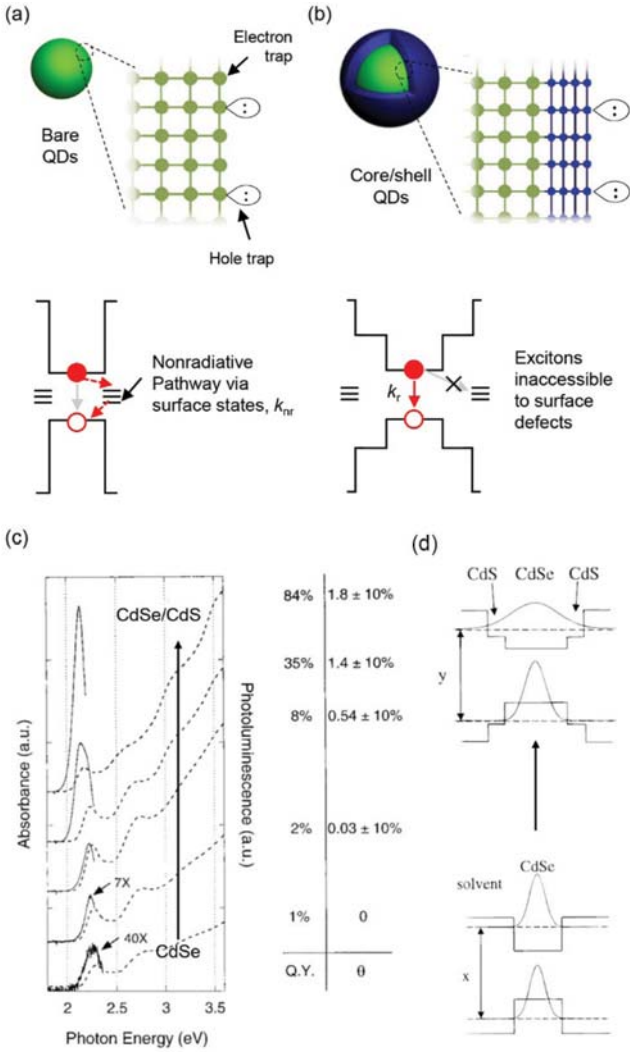

Fig. 4. Move Fig. 4 to the top of this page. (a) Synthesized QDs expose cationic or anionic unsaturated surface atoms at the solid-liquid interface where photogenerated electrons or holes are readily trapped (top). Localization of photogenerated carriers and their re- combination with other carriers lead to broad band surface state emission (photon energy <E_g) with very poor QY <1% or non-radiative decay, which reduces PL QY (bottom). (b) Heteroepitaxy of wide gap semiconductors on the core passivates the surface states and isolates the radiative decay of excitons from the surface states (top). As a result, the radiative recombination of excitons, corresponding to the energy of the band gap, can be improved (bottom). (c) Absorption (dashed line) and PL (solid line) spectra of CdSe (radius=1.5 nm)/CdS core/shell QDs with varied CdS shell coverage, θ (left). (d) Representation of electron and hole wavefunctions in CdSe core (lower right) and CdSe/CdS core/shell QDs (upper right) based on a particle-in-a-box model. Adapted with permission from Ref. [6]. Copyright 1997 American Chemical Society.

fied as nonradiative decay, k_{nr} (Fig. 4(a), red dashed arrows). Along with intrinsic radiative decay, k_r, the quantum yield can be expressed as the ratio of the intrinsic radiative decay rate to the overall decay rate (radiative and nonradiative): $\eta_{QY}=k_r/(k_r+k_{nr})$. According to this expression, there are two approaches for improving PL QY: increasing the radiative decay rate or decreasing the nonradiative decay rate. While the radiative decay rate is determined by the band gap and exciton fine structure ($1/k_r=\tau_r$=10-20 ns for CdSe QDs [35]) and generally regarded as an unchangeable intrinsic process, the nonradiative decay rate can be reduced by eliminating defect states. In over 20 years of QD research, the heteroepitaxy of wide band gap semiconductors (CdS, ZnSe, ZnS) on the emissive core (CdSe, CdS, InP, InAs), so-called core/shell heterostructures, has been a widely accepted approach for high QY [5-8,48-53]. The growth of the inorganic shell saturates the surface dangling bonds and constructs the type-I band gap structures that provide confinement potential for both electron and hole wavefunctions (Fig. 4(b)). Limited accessibility of excitons to dangling bonds on the shell therefore reduces the probability of nonradiative processes and consequently improves the PL QY. For example, Dabbousi et al. [6] demonstrated heteroepitaxy of the CdS shell on the CdSe core. Increasing CdS shell coverage (θ) by adding shell precursors leads to improved PL QY from 1% to 84% with a strong band-edge emission (Fig. 4(c)). We note that the fabrication of core/shell heterostructures reduces the optical band gap compared to the original core and is typical of core/shell heterostructures. This PL redshift is attributed to partial delocalization of exciton wavefunction to the shell region. According to a particle-in-a-box model with finite potential barriers, carrier wavefunctions in the quantum-confined box can tunnel into the potential wall, and the extent of tunneling depends on the height of the confinement potential. Compared to the organic ligands that provide quite high potential barriers due to their insulating nature, the shell materials only add 0.2-1.1 eV of potential barrier with respect to the cores (based on the bulk band gap position). In turn, tunneling of the carrier wavefunctions increases the effective size of the core and reduces the confinement energy (Fig. 4(c), right). Based on this fundamental design principle, various core/shell formulations with the type-I band gap configuration have been proposed: CdSe/ZnS [5], CdSe/ZnSe [50], InP/ZnS [54], and PbS/CdS [55].

While type-I core/shell heterostructures demonstrate the improved PL QYs, their fabrication does not always yield high quality QDs. In particular, core/ZnS QDs are the most desired core/shell pairs in terms of the largest confinement potential. The atomic profile of CdSe/ZnS core/shell QDs determined by McBride and co-workers [53] using Z-contrast scanning transmission electron microscopy (Z-STEM) revealed that adding ZnS shell precursors is likely to form non-spherical, irregular CdSe/ZnS heterostructures with a ZnS-dominant facet and/or unsaturated surface exposing CdSe, rather than spherical QD with homogeneous ZnS atomic layers. Such inhomogeneous shell growth is ascribed to the difference in surface reactivity between different facets (e.g., (110) and (001) facets in wurtzite crystal structures) and the lattice parameter between core and shell materials. For example, the difference in lattice parameters between CdSe (6.050 Å, zincblende) and ZnS (5.420 Å, zincblende) and accumulation of ZnS at a particular point applies compressive strain to CdSe cores and leads to the formation of internal defects such as misfit dislocation or point defects [5].

To overcome the difficulty of the homogeneous heteroexpitaxy of shells, more complex QD heterostructures employing lattice-adapting interlayers have been suggested [8,52,54,56,57]. For example, to establish gradual changes in the lattice parameter from core to shell and promote uniform shell growth, Talapin et al. [8] inserted a CdS or ZnSe layer between the CdSe core and ZnS shell. In these CdSe/CdS/ZnS and CdSe/ZnSe/ZnS double shell QDs, interlayers provided a stepwise change in the lattice constant (5.832 Å for CdS and 5.668 Å for ZnSe) as well as type-I band gap configuration to CdSe cores. Investigation of their morphology using STEM reveals a more homogeneous formation of the ZnS shell on the CdS interlayer [53]. This concept has been further elaborated to core/shell QDs with multiple and/or alloyed interlayers; for example, CdSe/CdS/$Cd_{0.5}Zn_{0.5}S$/ZnS core/multi-shell QDs [52] or CdSe/ZnS QDs with a CdSeZnS composition gradient at the interface [56]. These days, core/multi-shell heterostructures are a key design factor of various colloidal QDs for attaining high PL QY [58-61].

While the concept on core/shell heterostructures has been widely employed so far, lead halide perovskite QDs ($CH_3NH_3PbX_3$ or $CsPbX_3$, where X=Cl, Br, and I) exhibit very high PL QYs ranging from 50% to 90% without core/shell heterostructures. This unusual defect tolerance has been rationalized by computational study in which the surface atoms generate shallow traps (close to the CBM and VBM) or are resonant with VB and CB [62-64]. Qualitatively, the antibonding characteristics of VBM in the lead halide perovskites form non-bonding states associated with structural defects below the VBM [64] and CBM is stable due to strong spin-orbit coupling [65]. Despite the cleanness of the band gap, high dielectricity and corresponding small exciton binding energy (20-50 meV) [47,66] is likely to dissociate excitons and reduce the QY of perovskites. Therefore, to harness the photo and electrically generated carriers as photons, the perovskite materials need to be spatially confined as a form of nanocrystals to promote geminate recombination of excitons [62]. Many successful examples of perovskite-based QLEDs have adopted perovskites EMLs through in-situ nanocrystalline formation [62] or solution processing of colloidal perovskite QDs [67-70].

CORE/THICK SHELL QDs FOR REDUCED ENERGY TRANSFER

In typical QLEDs, the emissive layer is composed of 1-4 compact monolayers of QD films. In contrast to QD dispersion that separates QDs by more than tens of nanometers, densely packed QDs experience efficient energy transfer (ET) due to their proximity. Excitons in the QD can be transferred to other QDs in two ways: (1) photon emission from a QD and subsequent reabsorption by other QDs (emission and re-absorption) and (2) nonradiative Förster resonant energy transfer (FRET), which diffuses excitons in a QD to other proximal QDs without radiation events. Regardless of the physical mechanisms behind them, ET depends on the spectral overlap between PL of a donor (giving an exciton) and the absorption spectrum of an acceptor (receiving an exciton from a donor)

and their distance, d (ET rate ~$1/d^2$ for emission and re-absorption and rate ~$1/d^6$ for FRET). Because this event normally allocates higher energy excitons to lower energy states, PL resulting from ET is shifted to the lower energy side corresponding to the band gap of the accepter. For ideal QDs with a unity of QY, ET does not alter the QY of QD films because the ET event should be terminated by the radiative decay of excitons. However, typical QD samples exhibit QYs <1 as a result of a fraction of poorly passivated, defective QDs. Once an exciton is transferred to defective QDs (Fig. 5(a), grey QDs), the transferred exciton cannot generate a photon but loses its energy by heat. As a result, the QY of QD film should be less than that of QD dispersion and depresses the performance of QLEDs.

Fig. 5(b) displays the typical decay dynamics of CdSe/CdS core/shell QD films detected at the center, high energy side, and low energy side of the PL spectrum [71]. The upper left panel in Fig. 5(b) represents the typical spectroscopic behavior of QD films with moderate shell thickness (1-2 nm). Faster decay dynamics at the higher energy side (green arrows) than at the lower energy side (red arrows) represents the direction of energy transfer from high energy to low energy. Also, the overall decay dynamics of QD films are faster than those of QD dispersion due to the more rapid ET rate compared to the radiative decay rate of excitons. However, as the CdS shell thickness is increased (from upper left to lower right), the discrepancy between the QD solution and QD film becomes negligible; an increase in dot-to-dot spacing by the CdS shell from 4.2 nm to 13.8 nm almost fully suppresses the ET among QDs. This means that the energy transfer is so sensitive to dot-to-dot distance that increased shell thickness on several nanometer scales can effectively alleviate the ET between QDs. Employing these

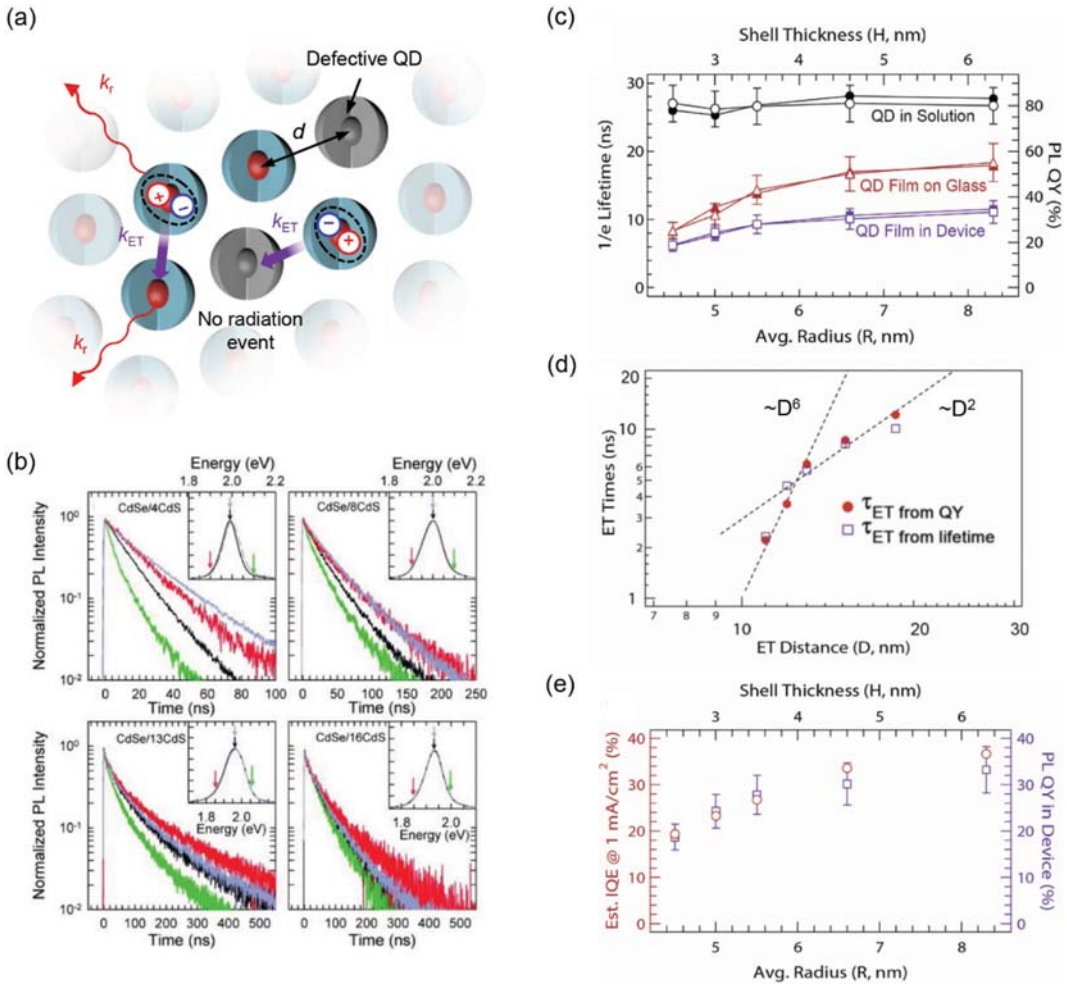

Fig. 5. (a) A schematic of the energy transfer among QDs in a densely packed QD emissive layer. Photo- or electrically generated excitons in QDs undergo radiative or non-radiative energy transfer (purple arrows, k_{ET}) from the donor QD with higher band gap to the acceptor QD with smaller band gap. If the acceptor QD is non-emissive due to internal/external defects (indicated as grey QDs), this acceptor QD loses the exciton by nonradiative decay (k_{nr}), not a photon generation (k_r). (b) Reduced energy transfer of CdSe/CdS QD films by increasing the CdS shell thickness from 4 monolayers to 16 monolayers. A thicker CdS shell reduces the discrepancy between solution PL decay and film PL decay and also minimizes the peak shift (insets). Adapted with permission from ref. [71]. Copyright 2012 American Chemical Society. (c) PL QYs and decay lifetimes of QDs (black) and QD films on glass (red) and in the device (blue). (d) ET time of QD films derived from PL QYs and decay lifetime. (e) Correlation between PL QY of QD films and internal quantum efficiency of QLEDs. Adapted with permission from ref. [23]. Copyright 2014 John Wiley and Sons.

CdSe/CdS thick shell QDs in QLEDs improves the peak EQE and maximum brightness of QLEDs; however, the degree of improvement is largely limited owing to their moderate PL QY and poor device structure [71].

Moreover, based on more advanced CdSe/CdZnS thick-shell QDs, Lim et al. demonstrated the close connectivity between the PL QY of QD films and the peak EQE of QLEDs [23]. QDs achieve high PL QY of over 80% due to the type-I band gap configuration that effectively protects exciton wavefunctions from the surface defects. Moreover, reduced lattice mismatch between a CdSe core and an alloyed CdZnS shell enables an increase in shell thickness by more than 8 nm. As shown in Fig. 5(c), PL QYs of QD films show clear dependence on shell thickness and become high with increasing shell thickness. Also, the decay lifetimes of QD films follow similar trends to those observed in a previous study [71]. Empirically, they related the PL QY of QD films and QD dispersions as follows: $Q_\infty=Q_0k_r/[(k_r+k_{ET}(1-Q_0)]$, where Q_0 is the PL QY of QD dispersion (without ET), Q_∞ is the PL QY of QD films (with ET), and k_r and k_{ET} are the radiative and ET rates, respectively. The ET time derived from this relationship reveals the ET mode of QD films as a function of shell thickness; for thin-shell QDs, the ET is dominated by FRET (depending on d^6) and changes with emission-reabsorption (depending on d^2) (Fig. 5(d)). More importantly, they revealed that the PL QYs of QD EMLs are essentially correlated with the IQE of QLEDs, assuming η_{out}=20% (Fig. 5(e)).

ENGINEERED CORE/SHELL INTERFACE TO SUPPRESS AUGER RECOMBINATION

A major difference between electrical pumping and optical pumping is that the excitation event does not always produce neutral electron-hole pairs. As illustrated in Fig. 2(a), the exciton formation of electrical pumping is made by separate injection of an electron and a hole under an applied bias. From the viewpoint of carrier tunneling, the charge injection rate depends on the potential barrier provided by a surface ligand layer, a wide band gap shell, the electric field across a QD EML, and the effective mass of the carriers. One can easily imagine that the complexity of a charge injection scheme involving material-dependent and device-dependent factors makes it very difficult to balance the electron and hole injection rate over a wide operation range; however, it can be achieved under limited conditions where the peak EQE appears. Rather than electron-hole pairs, the imbalanced charge injection introduces extra charges into the QDs. Because the emissive core of QDs in EMLs are electronically isolated by the shells, these extra carriers cannot be distributed to the entire EML or CTLs but remain in separate cores. Moreover, the formation of excitons in this QDs produces charged exciton, a combination of excitons and extra charges.

A signature of imbalanced charge injection in QLEDs was revealed by spectroscopic investigation of QD EMLs by Bae et al. [10] (Fig. 6(a) and 6(b)). In the inverted device structure adopting a ZnO ETL (widely used ETL in recent QLEDs), they observed voltage-dependent emergence of a fast decay component from the CdSe/CdS giant QD EML. Even without applied bias, QDs on a ZnO ETL exhibit a faster decay rate than those on a glass substrate. More importantly, increasing the applied bias further accelerates the decay

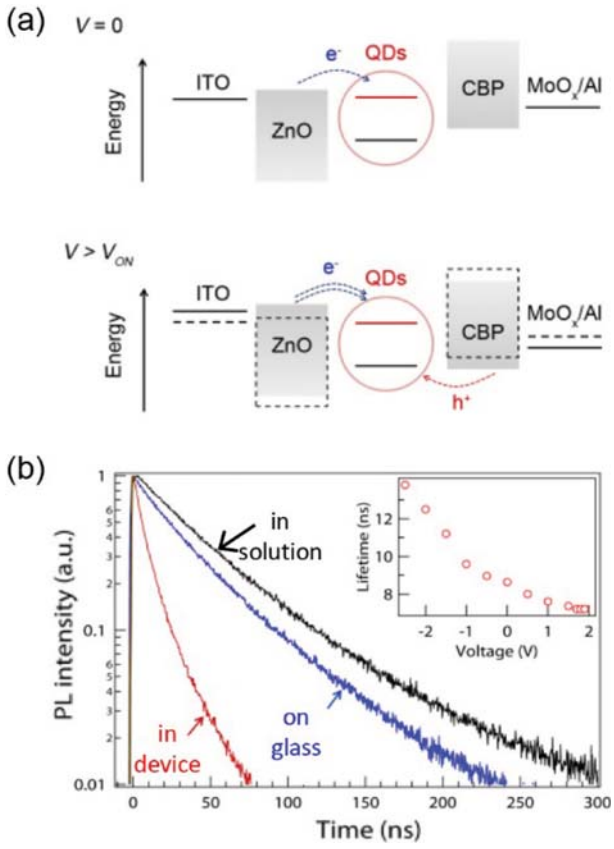

Fig. 6. (a) Spontaneous charging of QDs in ZnO ETL-based QLEDs. The Fermi level of ITO/ZnO is close to the CB of CdSe, which triggers spontaneous electron transfer from ITO/ZnO to QDs without applied bias (top). Under device operation, the electric field across the QD EML promotes extra electrons to QDs. As a result, the QDs are negatively charged. (b) Spectroscopic observation of negative charging of CdSe/CdS giant QDs in QLEDs. Compared to QDs on glass (slightly faster than dispersed QDs due to energy transfer), QDs in contact with ITO/ZnO exhibit a significant increase in the decay rate associated with the negative trion (two electrons and one hole in a QD). Inset displays the decrease in exciton lifetime under applied bias. Adapted with permission from ref. [10]. Copyright 2013 Nature Publishing Group.

rate of excitons (1/k~8.5 ns). This fast decay component corresponds to the negative trion (X^-), two electrons and one hole in QDs. They deduced that energetic proximity between the CB of QDs and the Fermi level of ITO/ZnO is responsible for negative charging of QDs, which spontaneously transfers electrons from ITO/ZnO to QDs. An increase in the applied bias accelerates the electron transfer from ITO/ZnO to QDs and EL from QLEDs is then dominated by negatively charged excitons, not neutral excitons. The negative trion QY is close to 0 for typical QDs; thus, QLEDs operated by those species should exhibit poor efficiency.

The presence of extra carriers in QDs opens ultrafast nonradiative recombination pathways of excitons known as Auger recombination [72]. This process transfers the recombination energy of excitons to other carriers and dissipates it as heat. In bulk semiconductors, this process is essentially ineffective and activated by

thermal energy because of strict translational momentum conservation. Namely, excitation of the third carrier to higher states in the parabolic dispersion curve accompanies a gain in the net momentum for the whole system, which violates the momentum conservation law [2]. However, spatial confinement of the carriers in QDs relaxes the translational momentum conservation to less strict angular momentum conservation and intensifies Coulombic interactions between charge carriers (see refs [72] and [2] for more details of Auger recombination in semiconductor nanocrystals). As a result,

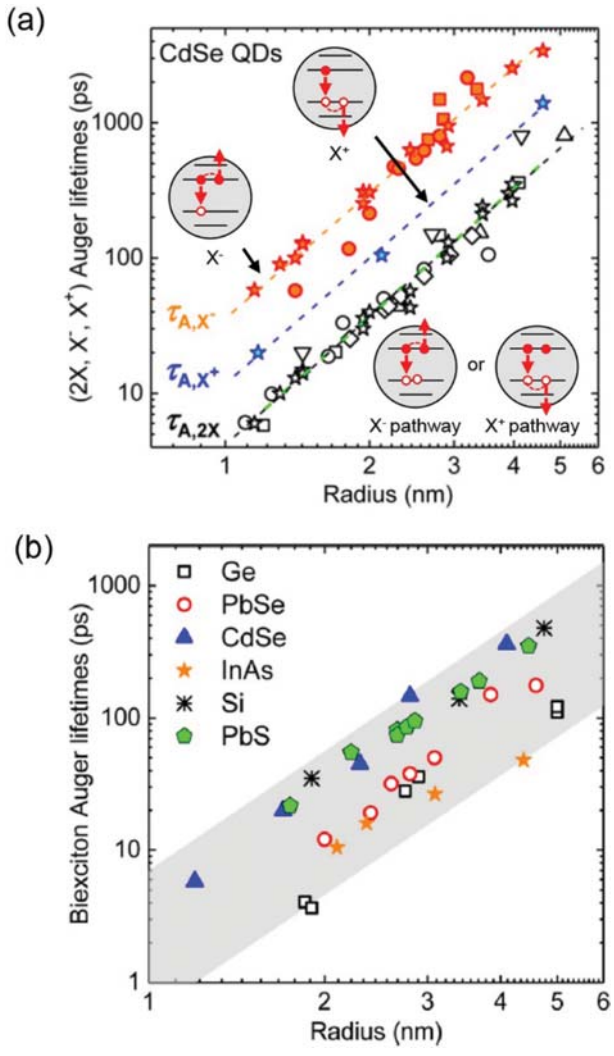

Fig. 7. (a) Auger lifetime of negative trions (X^-, two electrons and one hole), positive trions (X^+, one electron and two holes), and biexcitons (2X, two electrons and two holes) in CdSe QDs with different radii. Regardless of the number of Auger decay pathways, every series follows volume scaling (τ_A~1/r^3). (b) Universal volume scaling of the biexciton Auger lifetime for various direct (PbSe, PbS, CdSe, and InAs) or indirect (Si and Ge) band gap QDs. Despite different band gap and material-specific characteristics, biexciton Auger decay in QDs follows volume-dependent trends. Note that all data points range from several ps to hundreds of ps, which is far less than the intrinsic radiative recombination lifetime of excitons in QDs. Adapted with permission from ref. [2]. Copyright 2016 American Chemical Society.

Auger recombination in QDs is far more efficient than that in bulk. Compared to the intrinsic radiative decay of neutral excitons in CdSe QDs (~20 ns for wurtzite), the negative trion or biexciton Auger lifetime is 2-3 orders of magnitude faster (Fig. 7(a)). Consequently, the PL QY of charged excitons is less than 1%. We note that the Auger recombination of charged or multiexcitons is a universal phenomenon in various QDs and follows a size-related trend known as "volume scaling." Linear fits of the size-dependent Auger lifetime in log-log representation agree well with the relationship τ_A~1/r^m with m=3.13±0.1, regardless of negative trions, positive trions, or biexcitons [2] (Fig. 7(a)). This is widely observed in various direct and indirect band gap semiconductors [2] (Fig. 7(b)).

Controlling Auger recombination in QDs has been a major topic in QD research fields because of its relevance to practical devices utilizing multicarriers (e.g., lasers). Considering the origin of Auger recombination in QDs, increasing the QD volume may solve this issue; however, this results in the loss of band gap tunability by controlling the size, a major advantage of QDs. Auger recombination can be suppressed at low temperature but cannot be a practical solution because considerable suppression of Auger decay is only observed at cryogenic temperatures below 200 K [75].

To overcome the drawbacks of cryogenic condition or the loss of quantum confinement effect of colloidal QDs, instead, elaborate core/shell heterostructures have been studied, which directly tackle the transition probability of carriers involving Auger recombination. The Auger recombination process is divided into two electronic transitions; for example, for the negative trion: 1) recombination of one electron at CB and one hole at VB and 2) excitation of another electron by accepting the energy from 1). Thus, heterostructures hindering 1) and/or 2) can delay the Auger recombination rate. Manipulation of transition 1) has been achieved by reducing the overlap of electron-hole envelop wavefunctions using type-II (staggered band gap configuration, e.g., CdTe/CdSe [76,77] and CdS/ZnSe [78]) or quasi-type-II (providing a potential barrier only for one carrier, e.g., CdSe/CdS [73,79,80]) QDs. All these approaches increase the biexciton Auger lifetime to ~250 ps for CdSe/CdS or ~2 ns for CdTe/CdSe. However, the spatial separation of carriers also increases the single exciton lifetime to 100 s ns and makes η_{QY} susceptible to nonradiative channels.

Conversely, accessing the transition 2) by the smoothened confinement potential has been suggested by Cragg and Efros [81] and reexamined by Clemente et al. [82]. The probability of transition 2) is determined by the overlap between initial and final states of carriers involving the Auger process. In the Fourier-transformed vector space, the high energy final state occupies a narrow range of wavevectors, k. In contrast, the initial ground state is distributed over a wide range of k centered at k=0. A computational study revealed that the smoothened confinement potential decreases the distribution of ground state wavefunctions; consequently, it reduces the overlap between initial and final states involving Auger decay [81]. While the fabrication of smoothed confinement potential requires atomic scale control of the chemical composition at core/shell interfaces, this approach preserves electron-hole wavefunction overlap and exploits band gap tunability by size control.

The feasibility of the smoothened confinement potential in core/

shell QDs was demonstrated in a series of studies on CdSe/CdS giant QDs containing an unintentional CdSeS alloyed region at the core-shell interface [83]. Long-term CdS shell growth by successive ionic layer adsorption and reaction triggered interfacial diffusion between the CdSe core and CdS shell. Moreover, the presence of an alloyed interface was probed using a fluorescence line narrowing experiment that revealed the presence of phonon modes associated with CdSeS alloys [83]. As formation of the CdSeS alloyed interface became significant, they observed an increase of the biexciton Auger lifetime under increased pump fluences [83] and of the biexciton quantum yield (~40% on average, deduced from second-order correlation function measurement in single dot spectroscopy [84]). We note that several QDs gained an optimal smoothed interface at almost unity of the biexciton QY in single dot spectroscopy as a result of complete suppression of Auger recombination.

To apply this concept in a more reliable manner, Bae et al. demonstrated intentional control of the interfacial structure of CdSe/CdS QDs to reproduce the effect of the smoothened interface [73]. They employed an alloyed $CdSe_{0.5}S_{0.5}$ layer between the CdSe core and CdS shell (Fig. 8(a)). The $CdSe_{0.5}S_{0.5}$ layer reduced the abrupt change of VB confinement potential related to the trion pathway of Auger recombination. The suppressed Auger decay was revealed in ensemble ultrafast PL decay dynamics in which the biexciton lifetime increased by up to 1 ns (Fig. 8(b)) and the biexciton QY reached approximately 10%. Their approach was further developed by Park et al., who elaborated the smoothness of the confinement potential by increasing the chemical composition of Se in the $CdSe_xS_{1-x}$ alloyed layer, along with the radial direction, and improved the biexciton quantum yields up to ~30% [74]. In addition to exploring the optimal interface structure, they also decoupled the volume effect and interfacial effect. As discussed in Section 2, shaping the interface of core/shell QDs not only alters the smoothness of confinement, but also increases the effective volume of cores by delocalizing carrier wavefunctions. For instance, an increase in Se fraction in the $CdSe_xS_{1-x}$ alloyed layer from x=0.25 to 0.75 smooths the confinement potential but simultaneously increases the effective volume of the hole wavefunction from ~70 nm^3 to ~150 nm^3 (Fig. 8(c)). A comparative study of CdSe/CdS QDs with different core sizes (grey trace) and CdSe/CdSeS/CdS QDs with varying alloyed layer compositions (blue traces) reveals that both volume and interface effects contribute to the suppression of Auger recombination in these engineered QDs.

Adopting Auger-suppressed QDs in QLEDs indeed helps improve device efficiency as well as droop behavior. Bae et al. introduced conventional (CdSe/CdS) and engineered QDs (CdSe/CdSeS/CdS) to an inverted device structure and investigated the influ-

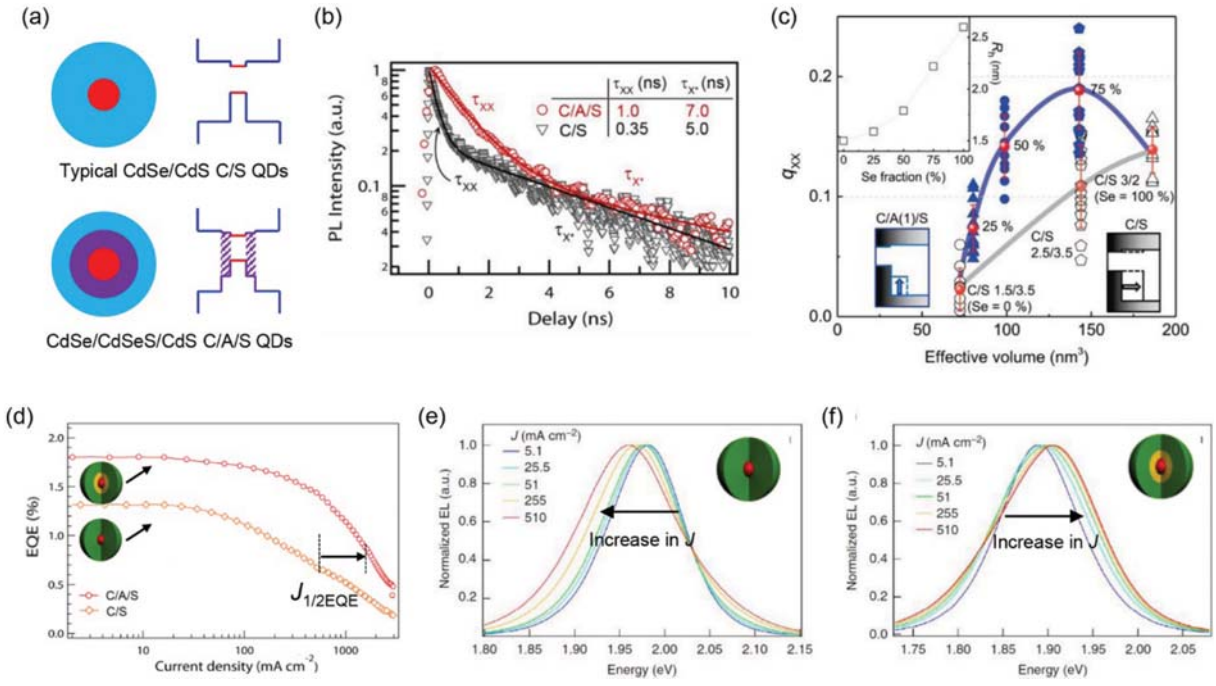

Fig. 8. (a) Schematic of conventional CdSe/CdS (C/S) QDs with sharp confinement potential (top) and engineered CdSe/CdSeS/CdS (C/A/S) QDs with smoothed confinement potential (bottom). The smoothed confinement potential is fabricated by introducing a CdSeS alloyed layer (purple region). (b) Multiexciton PL decay dynamics of C/A/S (red) and C/S (black) QDs. Biexciton and charged exciton lifetimes are listed in the inset. Adapted with permission from ref. [73]. Copyright 2013 American Chemical Society. (c) Biexciton quantum yield (q_{XX}) for C/S (grey) and C/A/S (blue) QDs with different effective excitonic volumes. Overall radius is fixed to 5 nm. Adapted with permission from ref. [74]. Copyright 2017 American Chemical Society. (d) EQE versus current density curves of C/S and C/A/S QDs. Suppressed Auger recombination of the negative trion improves the efficiency droop as well as the peak EQE. $J_{1/2EQE}$, a droop metric representing the current density at 50% EQE, is indicated for clarity. EL peak shift of (e) C/S and (f) C/A/S QDs for different driving currents. While conventional C/S QDs only exhibit the EL redshift due to Joule heating and the quantum confined Stark effect, C/A/S QDs display an EL blueshift with increasing current due to the contribution of emissive negative trions to EL. Adapted with permission from ref. [10]. Copyright 2013 Nature publishing group.

ence of QD heterostructures on device performance [10]. As addressed above, these QDs are prone to be charged due to spontaneous electron injection from ITO/ZnO. Compared to conventional QDs with negative trion QY≈0, interface-engineered QDs exhibit better peak EQEs (Fig. 8(d)) over the entire operational range. More importantly, they found that the Auger recombination of charged excitons is a major origin of the efficiency droop in QLEDs, and engineered core/shell QDs can relieve efficiency reduction by increasing negative trion QY. From observations of current-dependent EL spectra, while conventional QDs display an EL redshift with increasing current density due to Joule heating and the quantum confined Stark effect, engineered QDs exhibit a blueshift of EL spectra with increasing current density (Fig. 8(e)-8(f)). In CdSe/CdSeS/CdS QDs, negative trions have higher energy than neutral excitons due to Coulombic repulsion between electrons [85,86]; therefore, this unusual EL blueshift is direct evidence for the presence of negative trions and their contribution to EL. Reduced efficiency droop, quantified in this experiment using $J_{1/2EQE}$, which represents the current density reducing the peak EQE by 50%, is therefore attributed to the improved QY of negative trions.

Even though engineered QDs validate their benefits, avoiding QD charging would be a more essential solution to achieving high EQE, as demonstrated by state-of-the-art high efficiency QLEDs without Auger engineering [14,15,25]. Rather than low brightness applications such as indoor and mobile displays, it is believed that Auger-suppressed QDs will play a critical role in high power devices, which require high current density and consequent participation of charged or multiexcitons in EL. Lim et al. recently validated the optical gain of colloidal QDs under electrical pumping, a crucial precursor to laser action in devices [87]. In their achievement, continuously graded CdSe/$Cd_xZn_{1-x}Se$/ZnSeS QDs (so-called cg-QDs) showing highly suppressed Auger recombination (biexciton QY~ 50%) were the key element for maintaining population inversion at $1S_e$ and $1P_e$ states; otherwise, gain loss by Auger decay exceeded the rate of electrical pumping. To achieve high-power devices such as lasers, elaborate core/shell heterostructures with suppressed Auger decay will be a key engineering concept in the future.

SUMMARY AND OUTLOOK

Numerous studies introduced in this review have revealed a close relationship between the QY of QDs in devices and EL performance. As demonstrated by PL research, employing core/shell heterostructures has been an essential strategy for achieving high PL QY by preserving the radiative recombination of excitons against nonradiative pathways associated with surface states. Despite the similarity between PL and EL, however, the difference in pumping schemes (i.e., electronic transition occurring inside QDs versus separate, independent injection of carriers from outside QDs) and the nanoscopic morphology of QDs in emissive components (i.e., spatially separated composites versus close-packed, thin layers) generates additional efficiency-reducing phenomena, energy transfer among QDs, and the Auger recombination of charged excitons. These detrimental processes can be mitigated by elaborating the design of QD heterostructures. Energy transfer, intensified by the proximity of emitters, can be reduced by core/thick shell heterostructures that provide a sufficient dot-to-dot distance over ~10 nm. Formation of charged excitons and their nonradiative Auger recombination can be suppressed by adopting smoothened confinement potential at the core/shell interface. These tailored core/shell heterostructures of QDs will not only contribute to achieving highly efficient low brightness devices for displays, but also to realize high-power light emitting diodes or laser diodes in the future, as recently demonstrated by Lim et al. [87,88].

Even though vast progress has been made in QLEDs, there are several obstacles to be overcome before applying QLED technology on a practical level. The most critical constraint on QLEDs should be the use of heavy-metal QDs. Most QLEDs have introduced Cd- and Pb-based QDs as EMLs to exploit their extensive chemical library (e.g., various precursors, synthetic routes, and controllable reaction kinetics in multiple ways) and well-established physical properties. However, increasing demands for safe technology and regulations against harmful materials (e.g., Restriction on Hazardous Substance, RoHS [89]) will strongly restrict the use of heavy-metals. Although various candidates based on III-V (InP [58-60, 90], InAs [91-93], …), IV (Si [94-97]), and I-III-VI ($CuInSe_2$ [98-100], $CuInS_2$ [101-103], …) have been studied over the last 20 years, most alternatives do not match the practical performance metrics, such as QY, chemical- or photo-stability, and spectral narrowness of Cd- and Pb-based QDs. Only InP QDs have recently showed rapid progress (FWHM≤40 nm [104]) due to the huge demands of the display industry but still need further improvement for satisfying industrial standard for ultra-high definition displays (FWHM≤25 nm for Rec. 2020 [1]). Not only the environmental issue, but several technical hurdles such as long-term stability (particularly for blue), optical outcoupling, or reliable patterning process have also impeded to realize practical QLED applications. Most of them recently gains keen interests in the field of QLEDs but remains as open question.

Although heavy metal-based QDs are unable to be used in our daily life, they are still affordable to explore novel concepts overcoming various issues in QLEDs. For example, recent studies on the origin of operational instability of QLEDs by Jang et al. [105] and the quantitative analysis of exciton species in QLEDs [88] provide us profound insight on the operation mechanism of QLEDs and propose useful engineering guidelines to improve both efficiency and stability of QLEDs: a management of carrier injection rate for charge neutrality of excitons and a prevention of carrier leakage to adjacent carrier transport layers. In the meantime, II-VI anisotropic heterostructures have opened a new direction for designing better electroluminescence emitters. In recent articles by Oh et al. [106,107], dual heterojunction nanorods comprising CdSe QD-tipped CdS rod and ZnSe shell exhibit balanced and efficient charge injection. More importantly, in-plane transition dipole of nanorods allow for boosting outcoupling efficiency of LEDs more than 20% [107], while QLEDs require complicated optical structures inside and/or outside devices. Including the emission anisotropy of nanorods [107-109] or nanoplatelets [110], their enhanced radiative decay rate owing to the modified band-edge fine structures (see refs [111] for nanorods and refs [112-114] for nanoplatelets) and reduced Auger recombination rate [115] will be beneficial to minimize efficiency reduction by the formation of charged excitons.

In this review, we have mainly focused on the structural design of QDs and spectroscopic aspects of QLEDs. However, successful development of QLEDs requires comprehensive consideration and integration of relevant technologies, for example, the material development of device constituents (e.g., charge injection materials, charge transport materials, and emissive materials), the design of device architectures (e.g., arrangement of functional layers and assembly of unit devices for electronic integrity from unit devices to modules), and the fabrication processes (e.g., reliable and reproducible fabrication of unit device, integration with electric circuits, and defect-free micro processing). We believe that active contribution of chemical engineers will be highly demanded to solve various technical issues in this inclusive field such as the development of novel synthetic routes applying lessens from II-VI materials to greener alternatives (for example, wet chemistry of Ga and N for III-V QDs), the mass production of complicated QD heterostructures, purification, or the development of reliable fabrication processes, which will lead to the realization of environmentally safe, practical, and high performance QLEDs.

ACKNOWLEDGEMENT

This research was supported by the Basic Science Research Program through the National Research Foundation of Korea (NRF) funded by the Ministry of Education (NRF-2018R1D1A1B07047307) and the new faculty research fund of Ajou University.

REFERENCES

1. J. Lim, W. K. Bae, J. Kwak, S. Lee, C. Lee and K. Char, *Opt. Mater. Express*, **2**, 594 (2012).
2. J. M. Pietryga, Y.-S. Park, J. Lim, A. F. Fidler, W. K. Bae, S. Brovelli and V. I. Klimov, *Chem. Rev.*, **116**, 10513 (2016).
3. J. Chen, V. Hardev, J. Hartlove, J. Hofler and E. Lee, *SID Int. Symp. Dig. Tec.*, **43**, 895 (2012).
4. M. A. Hines and P. Guyot-Sionnest, *J. Phys. Chem.*, **100**, 468 (1996).
5. B. O. Dabbousi, J. Rodriguez-Viejo, F. V. Mikulec, J. R. Heine, H. Mattoussi, R. Ober, K. F. Jensen and M. G. Bawendi, *J. Phys. Chem. B*, **101**, 9463 (1997).
6. X. Peng, M. C. Schlamp, A. V. Kadavanich and A. P. Alivisatos, *J. Am. Chem. Soc.*, **119**, 7019 (1997).
7. D. V. Talapin, A. L. Rogach, A. Kornowski, M. Haase and H. Weller, *Nano Lett.*, **1**, 207 (2001).
8. D. V. Talapin, I. Mekis, S. Götzinger, A. Kornowski, O. Benson and H. Weller, *J. Phys. Chem. B*, **108**, 18826 (2004).
9. P. O. Anikeeva, C. F. Madigan, J. E. Halpert, M. G. Bawendi and V. Bulović, *Phys. Rev. B*, **78**, 085434 (2008).
10. W. K. Bae, Y.-S. Park, J. Lim, D. Lee, L. A. Padilha, H. McDaniel, I. Robel, C. Lee, J. M. Pietryga and V. I. Klimov, *Nat. Commun.*, **4**, 2661 (2013).
11. D. Bozyigit, O. Yarema and V. Wood, *Adv. Funct. Mater.*, **23**, 3024 (2013).
12. Y. Shirasaki, G. J. Supran, W. A. Tisdale and V. Bulović, *Phys. Rev. Lett.*, **110**, 217403 (2013).
13. B. S. Mashford, M. Stevenson, Z. Popovic, C. Hamilton, Z. Zhou, C. Breen, J. Steckel, V. Bulovic, M. Bawendi, S. Coe-Sullivan and P. T. Kazlas, *Nat. Photonics*, **7**, 407 (2013).
14. X. Dai, Z. Zhang, Y. Jin, Y. Niu, H. Cao, X. Liang, L. Chen, J. Wang and X. Peng, *Nature*, **515**, 96 (2014).
15. K. P. Acharya, A. Titov, J. Hyvonen, C. Wang, J. Tokarz and P. H. Holloway, *Nanoscale*, **9**, 14451 (2017).
16. L. Wang, J. Lin, Y. Hu, X. Guo, Y. Lv, Z. Tang, J. Zhao, Y. Fan, N. Zhang, Y. Wang and X. Liu, *ACS Appl. Mater. Interfaces*, **9**, 38755 (2017).
17. Y. Fu, W. Jiang, D. Kim, W. Lee and H. Chae, *ACS Appl. Mater. Interfaces*, **10**, 17295 (2018).
18. M. K. Choi, J. Yang, T. Hyeon and D.-H. Kim, *npj Flexible Electronics*, **2**, 10 (2018).
19. C.-Y. Han and H. Yang, *J. Korean Ceram. Soc.*, **54**, 449 (2017).
20. Y. Shirasaki, G. J. Supran, M. G. Bawendi and V. Bulović, *Nat. Photonics*, **7**, 13 (2012).
21. V. L. Colvin, M. C. Schlamp and A. P. Alivisatos, *Nature*, **370**, 354 (1994).
22. P. O. Anikeeva, J. E. Halpert, M. G. Bawendi and V. Bulović, *Nano Lett.*, **9**, 2532 (2009).
23. J. Lim, B. G. Jeong, M. Park, J. K. Kim, J. M. Pietryga, Y.-S. Park, V. I. Klimov, C. Lee, D. C. Lee and W. K. Bae, *Adv. Mater.*, **26**, 8034 (2014).
24. X. Li, Y.-B. Zhao, F. Fan, L. Levina, M. Liu, R. Quintero-Bermudez, X. Gong, L. N. Quan, J. Fan, Z. Yang, S. Hoogland, O. Voznyy, Z.-H. Lu and E. H. Sargent, *Nat. Photonics*, **12**, 159 (2018).
25. H. Shen, W. Cao, N. T. Shewmon, C. Yang, L. S. Li and J. Xue, *Nano Lett.*, **15**, 1211 (2015).
26. J. W. Stouwdam and R. A. J. Janssen, *J. Mater. Chem.*, **18**, 1889 (2008).
27. K.-S. Cho, E. K. Lee, W.-J. Joo, E. Jang, T.-H. Kim, S. J. Lee, S.-J. Kwon, J. Y. Han, B.-K. Kim, B. L. Choi and J. M. Kim, *Nat. Photon*, **3**, 341 (2009).
28. T.-H. Kim, K.-S. Cho, E. K. Lee, S. J. Lee, J. Chae, J. W. Kim, D. H. Kim, J.-Y. Kwon, G. Amaratunga, S. Y. Lee, B. L. Choi, Y. Kuk, J. M. Kim and K. Kim, *Nat. Photon*, **5**, 176 (2011).
29. J. Kwak, W. K. Bae, D. Lee, I. Park, J. Lim, M. Park, H. Cho, H. Woo, D. Y. Yoon, K. Char, S. Lee and C. Lee, *Nano Lett.*, **12**, 2362 (2012).
30. S. Jun, J. Lee and E. Jang, *ACS Nano*, **7**, 1472 (2013).
31. H. Woo, J. Lim, Y. Lee, J. Sung, H. Shin, J. M. Oh, M. Choi, H. Yoon, W. K. Bae and K. Char, *J. Mater. Chem. C*, **1**, 1983 (2013).
32. R. Meerheim, M. Furno, S. Hofmann, B. Lussem and K. Leo, *Appl. Phys. Lett.*, **97**, 253305 (2010).
33. A. L. Efros, M. Rosen, M. Kuno, M. Nirmal, D. J. Norris and M. Bawendi, *Phys. Rev. B*, **54**, 4843 (1996).
34. T. B. S. A. Crooker, *Appl. Phys. Lett.*, **82**, 2793 (2003).
35. D. J. Norris, A. L. Efros, M. Rosen and M. G. Bawendi, *Phys. Rev. B*, **53**, 16347 (1996).
36. J. K. L. M. Kuno, B. O. Dabbousi, F. V. Mikulec and M. G. Bawendi, *J. Chem. Phys.*, **106**, 9869 (1997).
37. M. Nirmal, D. J. Norris, M. Kuno, M. G. Bawendi, A. L. Efros and M. Rosen, *Phys. Rev. Lett.*, **75**, 3728 (1995).
38. L. Biadala, B. Siebers, Y. Beyazit, M. D. Tessier, D. Dupont, Z. Hens, D. R. Yakovlev and M. Bayer, *ACS Nano*, **10**, 3356 (2016).
39. A. Brodu, M. V. Ballottin, J. Buhot, E. J. van Harten, D. Dupont, A. La Porta, P. T. Prins, M. D. Tessier, M. Versteegh, V. Zwiller, S. Bals, Z. Hens, F. T. Rabouw, P. C. M. Christianen, C. de Mello Donega

and D. Vanmaekelbergh, *ACS Photonics*, **5**, 3353 (2018).
40. M. A. Becker, R. Vaxenburg, G. Nedelcu, P. C. Sercel, A. Shabaev, M. J. Mehl, J. G. Michopoulos, S. G. Lambrakos, N. Bernstein, J. L. Lyons, T. Stöferle, R. F. Mahrt, M. V. Kovalenko, D. J. Norris, G. Rainò and A. L. Efros, *Nature*, **553**, 189 (2018).
41. C. Adachi, M. A. Baldo, M. E. Thompson and S. R. Forrest, *J. Appl. Phys*., **90**, 5048 (2001).
42. Y. Ma, H. Zhang, J. Shen and C. Che, *Synth. Met*., **94**, 245 (1998).
43. M. A. Baldo, D. F. O'Brien, Y. You, A. Shoustikov, S. Sibley, M. E. Thompson and S. R. Forrest, *Nature*, **395**, 151 (1998).
44. K. Goushi, K. Yoshida, K. Sato and C. Adachi, *Nat. Photon*, **6**, 253 (2012).
45. A. Endo, K. Sato, K. Yoshimura, T. Kai, A. Kawada, H. Miyazaki and C. Adachi, *Appl. Phys. Lett*., **98**, 083302 (2011).
46. D. Yokoyama, Y. Setoguchi, A. Sakaguchi, M. Suzuki and C. Adachi, *Adv. Funct. Mater*., **20**, 386 (2010).
47. L. Protesescu, S. Yakunin, M. I. Bodnarchuk, F. Krieg, R. Caputo, C. H. Hendon, R. X. Yang, A. Walsh and M. V. Kovalenko, *Nano Lett*., **15**, 3692 (2015).
48. Y. Tian, T. Newton, N. A. Kotov, D. M. Guldi and J. H. Fendler, *J. Phys. Chem*., **100**, 8927 (1996).
49. L. Qu and X. Peng, *J. Am. Chem. Soc*., **124**, 2049 (2002).
50. P. Reiss, J. Bleuse and A. Pron, *Nano Lett*., **2**, 781 (2002).
51. J. J. Li, Y. A. Wang, W. Guo, J. C. Keay, T. D. Mishima, M. B. Johnson and X. Peng, *J. Am. Chem. Soc*., **125**, 12567 (2003).
52. R. Xie, U. Kolb, J. Li, T. Basché and A. Mews, *J. Am. Chem. Soc*., **127**, 7480 (2005).
53. J. McBride, J. Treadway, L. C. Feldman, S. J. Pennycook and S. J. Rosenthal, *Nano Lett*., **6**, 1496 (2006).
54. L. Li and P. Reiss, *J. Am. Chem. Soc*., **130**, 11588 (2008).
55. J. M. Pietryga, D. J. Werder, D. J. Williams, J. L. Casson, R. D. Schaller, V. I. Klimov and J. A. Hollingsworth, *J. Am. Chem. Soc*., **130**, 4879 (2008).
56. W. K. Bae, K. Char, H. Hur and S. Lee, *Chem. Mater*., **20**, 531 (2008).
57. S.-W. Kim, J. P. Zimmer, S. Ohnishi, J. B. Tracy, J. V. Frangioni and M. G. Bawendi, *J. Am. Chem. Soc*., **127**, 10526 (2005).
58. J. Lim, W. K. Bae, D. Lee, M. K. Nam, J. Jung, C. Lee, K. Char and S. Lee, *Chem. Mater*., **23**, 4459 (2011).
59. S. Kim, T. Kim, M. Kang, S. K. Kwak, T. W. Yoo, L. S. Park, I. Yang, S. Hwang, J. E. Lee, S. K. Kim and S.-W. Kim, *J. Am. Chem. Soc*., **134**, 3804 (2012).
60. J. Lim, M. Park, W. K. Bae, D. Lee, S. Lee, C. Lee and K. Char, *ACS Nano*, **7**, 9019 (2013).
61. E. Jang, S. Jun, H. Jang, J. Lim, B. Kim and Y. Kim, *Adv. Mater.*, **22**, 3076 (2010).
62. H. Cho, S.-H. Jeong, M.-H. Park, Y.-H. Kim, C. Wolf, C.-L. Lee, J. H. Heo, A. Sadhanala, N. Myoung, S. Yoo, S. H. Im, R. H. Friend and T.-W. Lee, *Science*, **350**, 1222 (2015).
63. H. Huang, M. I. Bodnarchuk, S. V. Kershaw, M. V. Kovalenko and A. L. Rogach, *ACS Energy Lett*., **2**, 2071 (2017).
64. M. V. Kovalenko, L. Protesescu and M. I. Bodnarchuk, *Science*, **358**, 745 (2017).
65. A. Swarnkar, V. K. Ravi and A. Nag, *ACS Energy Lett*., **2**, 1089 (2017).
66. V. D'Innocenzo, G. Grancini, M. J. P. Alcocer, A. R. S. Kandada, S. D. Stranks, M. M. Lee, G. Lanzani, H. J. Snaith and A. Petrozza, *Nat. Commun*., **5**, 3586 (2014).
67. T. Chiba, K. Hoshi, Y.-J. Pu, Y. Takeda, Y. Hayashi, S. Ohisa, S. Kawata and J. Kido, *ACS Appl. Mater. Interfaces*, **9**, 18054 (2017).
68. J. Li, L. Xu, T. Wang, J. Song, J. Chen, J. Xue, Y. Dong, B. Cai, Q. Shan, B. Han and H. Zeng, *Adv. Mater*., **29**, 1603885 (2017).
69. K. Hoshi, T. Chiba, J. Sato, Y. Hayashi, Y. Takahashi, H. Ebe, S. Ohisa and J. Kido, *ACS Appl. Mater. Interfaces*, **10**, 24607 (2018).
70. F. Yan, J. Xing, G. Xing, L. Quan, S. T. Tan, J. Zhao, R. Su, L. Zhang, S. Chen, Y. Zhao, A. Huan, E. H. Sargent, Q. Xiong and H. V. Demir, *Nano Lett*., **18**, 3157 (2018).
71. B. N. Pal, Y. Ghosh, S. Brovelli, R. Laocharoensuk, V. I. Klimov, J. A. Hollingsworth and H. Htoon, *Nano Lett*., **12**, 331 (2012).
72. V. I. Klimov, *Annu. Rev. Condens. Matter Phys*., **5**, 285 (2014).
73. W. K. Bae, L. A. Padilha, Y.-S. Park, H. McDaniel, I. Robel, J. M. Pietryga and V. I. Klimov, *ACS Nano*, **7**, 3411 (2013).
74. Y.-S. Park, J. Lim, N. S. Makarov and V. I. Klimov, *Nano Lett.*, **17**, 5607 (2017).
75. C. Javaux, B. Mahler, B. Dubertret, A. Shabaev, A. V. Rodina, A. L. Efros, D. R. Yakovlev, F. Liu, M. Bayer, G. Camps, L. Biadala, S. Buil, X. Quelin and J. P. Hermier, *Nat. Nanotechnol*., **8**, 206 (2013).
76. P. T. K. Chin, C. de Mello Donegá, S. S. van Bavel, S. C. J. Meskers, N. A. J. M. Sommerdijk and R. A. J. Janssen, *J. Am. Chem. Soc.*, **129**, 14880 (2007).
77. D. Oron, M. Kazes and U. Banin, *Phys. Rev. B*, **75**, 035330 (2007).
78. S. A. Ivanov, A. Piryatinski, J. Nanda, S. Tretiak, K. R. Zavadil, W. O. Wallace, D. Werder and V. I. Klimov, *J. Am. Chem. Soc.*, **129**, 11708 (2007).
79. Y. Chen, J. Vela, H. Htoon, J. L. Casson, D. J. Werder, D. A. Bussian, V. I. Klimov and J. A. Hollingsworth, *J. Am. Chem. Soc.*, **130**, 5026 (2008).
80. B. Mahler, P. Spinicelli, S. Buil, X. Quelin, J.-P. Hermier and B. Dubertret, *Nat. Mater*., **7**, 659 (2008).
81. G. E. Cragg and A. L. Efros, *Nano Lett*., **10**, 313 (2010).
82. J. I. Climente, J. L. Movilla and J. Planelles, *Small*, **8**, 754 (2012).
83. F. García-Santamaría, S. Brovelli, R. Viswanatha, J. A. Hollingsworth, H. Htoon, S. A. Crooker and V. I. Klimov, *Nano Lett.*, **11**, 687 (2011).
84. Y. S. Park, A. V. Malko, J. Vela, Y. Chen, Y. Ghosh, F. García-Santamaría, J. A. Hollingsworth, V. I. Klimov and H. Htoon, *Phys. Rev. Lett*., **106**, 187401 (2011).
85. V. I. Klimov, S. A. Ivanov, J. Nanda, M. Achermann, I. Bezel, J. A. McGuire and A. Piryatinski, *Nature*, **447**, 441 (2007).
86. A. Piryatinski, S. A. Ivanov, S. Tretiak and V. I. Klimov, *Nano Lett.*, **7**, 108 (2007).
87. J. Lim, Y.-S. Park and V. I. Klimov, *Nat. Mater*., **17**, 42 (2017).
88. J. Lim, Y.-S. Park, K. Wu, H. J. Yun and V. I. Klimov, *Nano Lett.*, **18**, 6645 (2018).
89. T. E. Parliament, Directive 2011/65/EU of the European Parliament and of the Council of 8 June 2011 on the restriction of the use of certain hazardous substances in electrical and electronic equipment, <http://eur-lex.europa.eu/legal-content/EN/TXT/?qid=1399998664957&uri=CELEX:02011L0065-20140129> (2011).
90. T. Kim, S. W. Kim, M. Kang and S.-W. Kim, *J. Phys. Chem. Lett.*, **3**, 214 (2011).
91. Y. W. Cao and U. Banin, *Angew. Chem. Int. Ed*., **38**, 3692 (1999).
92. Y. Cao and U. Banin, *J. Am. Chem. Soc.*, **122**, 9692 (2000).

93. S.-W. Kim, J. P. Zimmer, S. Ohnishi, J. B. Tracy, J. V. Frangioni and M. G. Bawendi, *J. Am. Chem. Soc.*, **127**, 10526 (2005).
94. Z. Kang, Y. Liu, C. H. A. Tsang, D. D. D. Ma, X. Fan, N.-B. Wong and S.-T. Lee, *Adv. Mater.*, **21**, 661 (2009).
95. J. Zou, R. K. Baldwin, K. A. Pettigrew and S. M. Kauzlarich, *Nano Lett.*, **4**, 1181 (2004).
96. D. S. English, L. E. Pell, Z. Yu, P. F. Barbara and B. A. Korgel, *Nano Lett.*, **2**, 681 (2002).
97. J. D. Holmes, K. J. Ziegler, R. C. Doty, L. E. Pell, K. P. Johnston and B. A. Korgel, *J. Am. Chem. Soc.*, **123**, 3743 (2001).
98. H. McDaniel, A. Y. Koposov, S. Draguta, N. S. Makarov, J. M. Pietryga and V. I. Klimov, *J. Phys. Chem. C*, **118**, 16987 (2014).
99. E. Witt and J. Kolny-Olesiak, *Chem. Eur. J.*, **19**, 9746 (2013).
100. H. McDaniel, N. Fuke, J. M. Pietryga and V. I. Klimov, *J. Phys. Chem. Lett.*, **4**, 355 (2013).
101. L. Li, T. J. Daou, I. Texier, T. T. Kim Chi, N. Q. Liem and P. Reiss, *Chem. Mater.*, **21**, 2422 (2009).
102. J. Park and S.-W. Kim, *J. Mater. Chem.*, **21**, 3745 (2011).
103. B. Chen, H. Zhong, W. Zhang, Z. a. Tan, Y. Li, C. Yu, T. Zhai, Y. Bando, S. Yang and B. Zou, *Adv. Funct. Mater.*, **22**, 2081 (2012).
104. P. Ramasamy, N. Kim, Y.-S. Kang, O. Ramirez and J.-S. Lee, *Chem. Mater.*, **29**, 6893 (2017).
105. J. H. Chang, P. Park, H. Jung, B. G. Jeong, D. Hahm, G. Nagamine, J. Ko, J. Cho, L. A. Padilha, D. C. Lee, C. Lee, K. Char and W. K. Bae, *ACS Nano*, **12**, 10231 (2018).
106. N. Oh, S. Nam, Y. Zhai, K. Deshpande, P. Trefonas and M. Shim, *Nat. Commun.*, **5**, 3642 (2014).
107. S. Nam, N. Oh, Y. Zhai and M. Shim, *ACS Nano*, **9**, 878 (2015).
108. A. Rizzo, C. Nobile, M. Mazzeo, M. D. Giorgi, A. Fiore, L. Carbone, R. Cingolani, L. Manna and G. Gigli, *ACS Nano*, **3**, 1506 (2009).
109. R. A. M. Hikmet, P. T. K. Chin, D. V. Talapin and H. Weller, *Adv. Mater.*, **17**, 1436 (2005).
110. D.-E. Yoon, W. D. Kim, D. Kim, D. Lee, S. Koh, W. K. Bae and D. C. Lee, *J. Phys. Chem. C*, **121**, 24837 (2017).
111. P. C. Sercel and A. L. Efros, *Nano Lett.*, **18**, 4061 (2018).
112. L. T. Kunneman, J. M. Schins, S. Pedetti, H. Heuclin, F. C. Grozema, A. J. Houtepen, B. Dubertret and L. D. A. Siebbeles, *Nano Lett.*, **14**, 7039 (2014).
113. L. Biadala, F. Liu, M. D. Tessier, D. R. Yakovlev, B. Dubertret and M. Bayer, *Nano Lett.*, **14**, 1134 (2014).
114. S. Ithurria, M. D. Tessier, B. Mahler, R. P. S. M. Lobo, B. Dubertret and A. L. Efros, *Nat. Mater.*, **10**, 936 (2011).
115. H. Htoon, J. A. Hollingsworth, R. Dickerson and V. I. Klimov, *Phys. Rev. Lett.*, **91**, 227401 (2003).

Jaehoon Lim is Assistant Professor within the department of chemical engineering and the department of energy system research in Ajou University, South Korea. He obtained B.S. (2007) and Ph. D. (2013) in Chemical and Biological Engineering from Seoul National University. He conducted postdoctoral research work within the Department of Electrical Engineering and Computer Science at Seoul National University (2013-2014) and within the Chemistry Division of Los Alamos National Laboratory (2013-2017). His current research centers on the synthesis and characterization of colloidal semiconductor nanocrystals and their applications in light-emitting diodes, lasing, solar energy conversion, and sensing.